

Turbulence and inertial effects in a porous bed: DNS and flow analysis

By X. He[†], S. Apte[‡], K. Schneider[‡], B. Kadoch[‡] AND M. Farge[¶]

Direct numerical simulation (DNS) of pore-scale turbulence is performed in a unit cell of a face-centered cubic lattice at three different pore Reynolds numbers (300, 500 and 1000). Eulerian statistics of mean and fluctuating velocity field, turbulent kinetic energy (TKE) budget, and single and two-point correlations are obtained to quantify the effect of confinement on turbulence in porous media. Large acceleration and deceleration regions in the flow field yield negative TKE production and flow features similar to a jet-impingement-like flow. The flow field is also analyzed using angular Lagrangian statistics (Bos *et al.* 2015) of fluid particles to study the temporal evolution of the direction change and its asymptotic behavior, the latter being hypothesized to be dependent on the pore geometry. A stochastic Monte Carlo-based model is developed to provide a reasonable prediction of this asymptotic curvature angle. The Eulerian and Lagrangian correlations are used to characterize pore-scale dispersion.

1. Introduction

Packed bed reactors are routinely used for synthesis of basic chemicals and intermediates in the chemical and process industries. Random packing of porous media is one of the arrangements used in practice that exhibit typical flow Reynolds number on the order of 1000 or more. This results in inertial effects and turbulence within pore space which, together with resultant dispersion properties, plays a critical role in the transport of reactants and products to and from active reaction sites. Contrary to conventional thought about low-speed fluid flow in porous media, the inertial contribution to the flow field is often important in applications, and the inertial terms can dramatically change the topology of the flow field (such as formation of jets, vortexes, dead zones, etc. within pores). However, the mechanisms of how inertial and turbulent flows affect the large-scale friction factor are poorly understood (Hlushkou & Tallarek 2006).

Furthermore, nearly all theoretical studies of dispersion in porous media have been on the condition of either (i) Stokes flow (which neglects the influence of inertial contributions completely), or (ii) inertial flow without any turbulence effects. Researchers typically rely on established empirical correlations for predicting transport and dispersive properties of flow in fixed beds and ultimately in reactor design (Andrigo *et al.* 2000; Eigenberger 1992). Development of Reynolds-averaged Navier Stokes (RANS) models for flow at the pore-scale level has been attempted by numerous researchers (for instance in Lemos & Pedras (2001); Pearson & Tardy (2002)). For example, the RANS $k-\epsilon$ model has been derived by time averaging the volume-averaged extended Darcy-Forchheimer model equations (Antohe & Lage 1997), or by volume averaging the time-averaged Reynolds-averaged equation (Masuoka & Takatsu 1996; Nakayama & Kuwahara 1999; Suga 2016),

[†] Department of Mechanical Engineering, Oregon State University

[‡] Aix-Marseille Université, France

[¶] Ecole Normale Supérieure, France

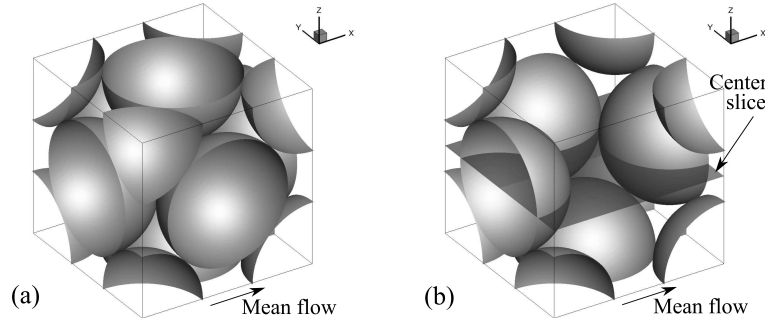


FIGURE 1. (a) Geometry of face-centered porous unit cell, (b) same as (a) except some beads are removed so that the flow region inside of unit cell can be observed.

or by the double-decomposition technique developed based on exchangeability of volume-time or time-volume averaging (Pedras & Lemos 2001). In these models, extra terms requiring closure are obtained by conducting numerical experiments on simple geometries such as a periodic array of rods and by using standard turbulence closure techniques based on a gradient diffusion hypothesis. However, these models lack validation with experimental or DNS data. A majority of these models predict non-zero Reynolds stress for laminar flows (Pope 2000), making them inconsistent for applications over the full range of Re from laminar to turbulent flows.

For high Re flows through porous media, several fundamental questions related to the structure and characteristics of turbulence remain. There is currently seldom PIV or DNS data on pore-scale flow characterization. In particular, measurement of shear stresses, the spectrum of turbulent kinetic energy, the characteristics of near-wall flow structures, inertial structures (such as jets and wakes), and velocity correlation functions (Patil & Liburdy (2013) studied this but on a two-dimensional domain using PIV measurements) would be useful quantities to measure in porous media. Currently, only global macroscopic parameters (pressure drop, longitudinal dispersion) have been measured; some empirical correlations exist for these quantities (Ergun 1952; Dixon & Cresswell 1986; Gunn 1987; Wen & Fan 1975).

To answer the remaining questions and overcome the drawbacks of the current models, direct numerical simulation is performed in this work. The spatio-temporal velocity and pressure data are used to analyze Eulerian and Lagrangian correlations. Detailed Lagrangian analysis of the curvature angle is performed to study the influence of bed confinement on turbulence statistics. Section 2 provides the details of the porous scale geometry, simulation parameters and numerical approach. Section 3 presents some key results on Eulerian statistics and correlations. Lagrangian correlations together with curvature angle statistics and a stochastic model are described in Section 4. Finally, a summary of the results is given in Section 5.

2. Computational geometry and simulation parameters

A porous face-centered cubic (FCC) unit cell (Figure 1) is used in this work. It has a half sphere entering at each face of the cube, and a quarter sphere at each corner. The face-centered cubic arrangement results in the lowest possible porosity (ϕ), the ratio of the void volume (V_{void}) to the total volume (V_{total}), equal to 0.26. Due to the extreme compactness, the flow through the unit cell experiences rapid expansion and contraction, where the turbulence effects are intensified.

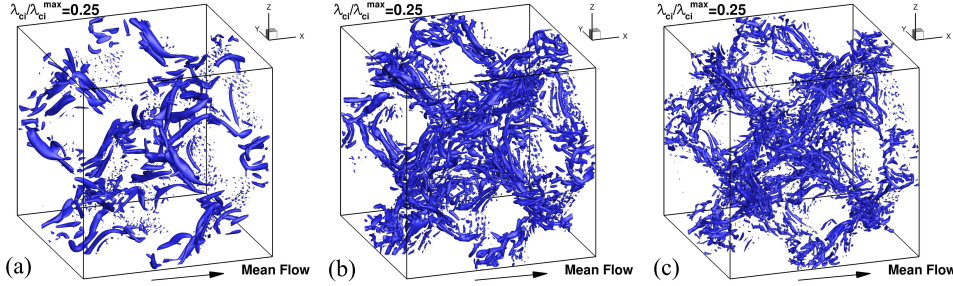


FIGURE 2. Iso-surface of swirling strength $\lambda_{ci} = 0.25\lambda_{ci}^{max}$ at (a) $Re_p = 300$, (b) $Re_p = 500$ and (c) $Re_p = 1000$.

Hill & Koch (2002) studied the same geometry using the lattice-Boltzmann method for flows up to $Re_p = 300$, and pore Reynolds number (Re_p) is defined with the adoption of porosity as

$$Re_p = \frac{U_{int} D_B}{\nu} \frac{\phi}{1 - \phi}, \quad (2.1)$$

where, U_{int} is the interstitial velocity of flow in porous media, D_B the bead diameter, and ν the kinematic viscosity of fluid. In this work, the flow at three pore Reynolds numbers ($Re_p = 300, 500$ and 1000) is simulated using direct numerical simulation, ranging from unsteady inertial to turbulent regions. A periodic boundary condition is specified at all faces. According to Hill & Koch (2002), the flow is driven by pressure gradient, which can be written in the form of a body force

$$F = 365 + 10.9 Re_p \quad (27 < Re_p < 216). \quad (2.2)$$

$$F = 462 + 9.85 Re_p \quad (Re_p \geq 216). \quad (2.3)$$

A fictitious domain method developed by Apte *et al.* (2008) is applied to confront the challenge of the complex packed-bed geometry. Uniform Cartesian grids are used in the entire simulation domain, including both fluid and solid phases. An additional body force is imposed on the solid part to enforce the rigid body motion and satisfy the no-slip boundary condition. The absence of highly skewed unstructured mesh at the bead surface is likely to accelerate the convergence and lower the uncertainty (Justin & Apte 2013). The following governing equations are solved over the entire domain, including the region within the solid bed, and a rigidity constraint force, \mathbf{f} , is applied that is non-zero only in the solid region.

$$\nabla \cdot \mathbf{u} = 0 \quad (2.4)$$

$$\rho_\gamma \left[\frac{\partial \mathbf{u}}{\partial t} + (\mathbf{u} \cdot \nabla) \mathbf{u} \right] = -\nabla p + \mu_\gamma \nabla^2 \mathbf{u} + \rho_\gamma \mathbf{g} + \mathbf{f}, \quad (2.5)$$

where \mathbf{u} is the velocity vector (with components given by $\mathbf{u} = (u_x, u_y, u_z)$), ρ_γ the fluid density, μ_γ the fluid viscosity, p the pressure, and \mathbf{g} the gravitational acceleration.

3. Eulerian statistics and discussion

In order to answer some fundamental questions about inertial and turbulent flow in packed beds, such as how the local pore velocity structure affects the turbulent intensity, homogeneity and isotropicity, what the dominant mechanisms are for turbulent kinetic energy production, dissipation and diffusion, time-averaged turbulent kinetic en-

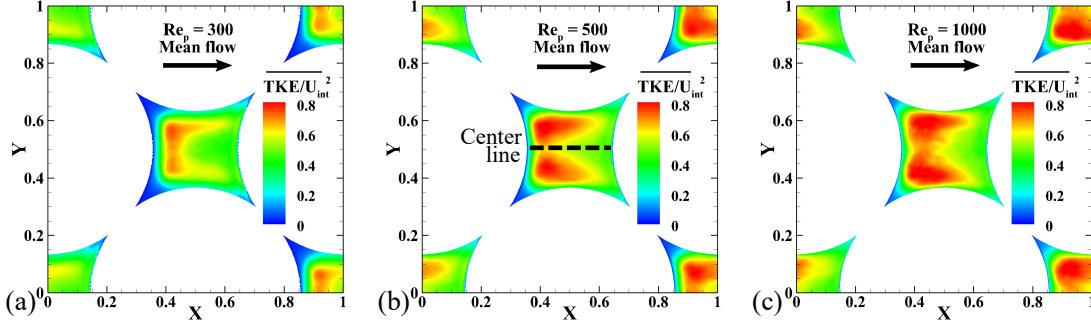


FIGURE 3. Contour of normalized TKE distribution on the center slice of the unit cell for (a) $Re_p = 300$, (b) $Re_p = 500$ and (c) $Re_p = 1000$.

ergy (TKE) distribution are collected, TKE budgets are calculated explicitly, as well as the local swirling strength λ_{ci} (Zhou *et al.* 1998).

3.1. Vortical structure visualization

To determine how the flow structures are influenced by the local mean velocity field, the local swirling strength λ_{ci} is computed to visualize the vortical structures at three different Reynolds numbers. It is calculated as the imaginary part of the complex conjugate eigenvalue of the velocity gradient tensor. Isosurfaces for 25% of the local maximum value of λ_{ci} are used to visualize local swirling structures. In Figure 2, it is observed that the size of vortices in the streamwise direction is becoming smaller with higher Re_p , implying that at a fully turbulent region, the flow is less correlated in the specific direction compared to that in an unsteady inertial region. This observation is consistent with the theory that the integral length scale will decrease with increasing Re_p in turbulent flows. In the spanwise directions, similar trend is observed, but it is not as pronounced. Moreover, in each Reynolds number case, the size and connectivity of vortices located at distinct parts of unit cell are quite different, suggesting the presence of high anisotropy. Thus, a visualization of the anisotropy Reynolds stress tensor is required in future analyses.

3.2. TKE and its budgets

The time-averaged TKE distribution on the center slice of the unit cell (see Figure 1(b)) is shown in Figure 3. The contours are normalized by U_{int}^2 , where U_{int} is the interstitial velocity. It can be observed that the turbulent intensity is increasing with higher Re_p , and TKE is distributed in a specific pattern in the center pore region for all three Reynolds numbers. To better understand the mechanism of TKE transport in pore-scale, production, dissipation and all the other terms in the TKE transport equation are explicitly calculated (Pope 2000). Because there is no homogeneous direction in the porous geometry, the budgets along the center line are plotted for $Re_p = 500$ (Figure 3(b)). All the budget terms are distinguished in Figure 4(a), except the local unsteady term, which is zero for stationary flows.

Several conclusions can be drawn from Figure 4(a) that are described in what follows. The first conclusion is that negative production (solid line with filled circle) is obtained near the entrance and exit of the center pore region. In most situations, the production term should remain positive, implying that the mean flow is supporting turbulence. However, if the production becomes negative, the energy transport process is reversed. Turbulence is actually providing energy and feeding the mean flow. Such a phenomenon

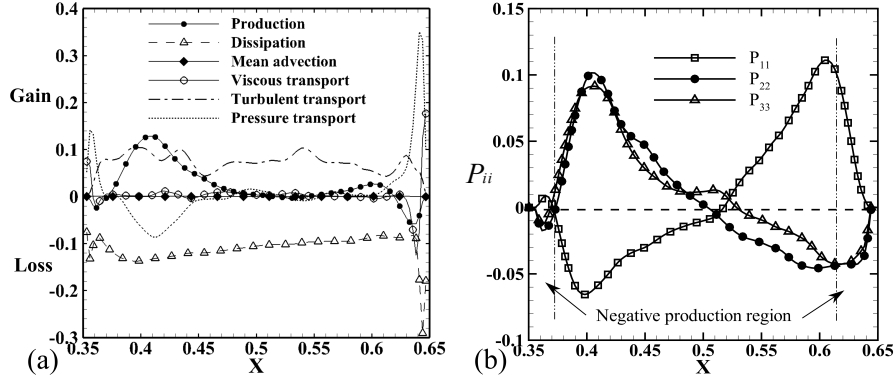


FIGURE 4. (a) TKE budget of $Re_p = 500$ along the center line and (b) normal components of production term.

is rare, and it cannot be reproduced using any types of RANS models with the same geometry.

The mechanism of negative production at near wall regions can be explained in Figure 4(b). Along the center line, normal components of production, P_{ii} , are dominant. In the negative production regions, the spanwise components, P_{22} and P_{33} , become negative while the streamwise component, P_{11} , is positive. Production is defined as the negative product of Reynolds stress $\overline{u_i' u_k'}$ multiplied by the mean strain rate $\frac{\partial \overline{u_i}}{\partial x_k}$, where the normal components of Reynolds stress $\overline{u_i'^2}$ are always positive. Hence the sign is decided by the mean strain rate $\frac{\partial \overline{u_i}}{\partial x_i}$.

The exit region is discussed first, as it is easier to explain. As shown in Figures 1(b) and 3, after the flow enters the center pore, it will first accelerate and then decelerate due to the complex confinement. After it travels across the major part of the pore, some part of the flow will hit the bead surface, similar to an impinging jet, and then merge with the rest and exit the pore through the crevices. During this process, the flow is accelerating in the spanwise directions, while decelerating in the streamwise directions. As a result, the mean strain rate in y and z directions becomes positive, but negative in the x direction. Together with the positive normal Reynolds stress, the production term now can be decomposed completely. To summarize, the sum of negative production in the spanwise directions outnumbers that in the streamwise direction, which causes the net production to be negative near the center pore exit region. Nishino *et al.* (1996) reported that, where a particle-tracking velocimetry (PTV) experiment was carried out for an impinging jet, negative production was also observed near the stagnation zone similar to what has been described here.

As for the entrance region, the mechanism is similar except that there is no jet impingement. The flow goes into the pore through the cleavages on the sides of the unit cell and merges at the initial part of the center pore. That is to say, it is accelerating in the spanwise directions too. But in the streamwise direction, the scenario becomes complicated. A recirculation zone near the crest is created by the merging flow, which leads to the negative mean strain rate in x direction.

The second conclusion is that the turbulent transport term (dash-dotted line) is large over most of the pore region. This is quite different from what is obtained in turbulent channel flows, where the turbulent transport term only becomes substantial in the near-wall region. According to Figure 3, a large amount of TKE is generated and distributed

all over the pore. Moreover, it is redistributed by Reynolds stress working with fluctuating velocity.

Lastly, the third conclusion is that production is not equal to dissipation (dashed line with unfilled triangle) in most of the flow domain, which means that most of turbulence in porous media is not at equilibrium state. This implies that RANS models, all based on the gradient-diffusion hypothesis, may be unable to predict accurate solutions in such circumstances.

4. Angular multiscale statistics and a stochastic model

The porous geometric effects on the flow structures have received much attention recently (Bos *et al.* 2015; Uth *et al.* 2016). Angular multiscale statistics of fluid particle trajectories (Bos *et al.* 2015) are obtained to quantify the effect of confinement on the flow. Following a fluid particle in the Lagrangian frame, an angle, Θ , formed by consecutive particle locations (see Figure 5(a)), is related to the curvature of the fluid particle paths. To calculate this angle, three equal-time span points along the trajectory are used, and Θ is defined as the angle between two position vectors constructed consecutively by these three points using the following equation,

$$\cos[\Theta(t, \tau)] = \frac{\delta X(\mathbf{x}(t_0), t, \tau) \cdot \delta X(\mathbf{x}(t_0), t + \tau, \tau)}{|\delta X(\mathbf{x}(t_0), t, \tau)| |\delta X(\mathbf{x}(t_0), t + \tau, \tau)|}, \quad (4.1)$$

where $\delta X = X(x_0, t) - X(x_0, t - \tau)$ is the spatial increment and $X(x_0, t)$ is the position of a fluid particle at time t , which is initially injected at x_0 . The cosine of the angle describes the directional change with time lag and thus characterizes the multiscale feature of turbulent flows. As discussed in Bos *et al.* (2015), at short time spans, the curvature angle is linearly proportional to the time lag, with the constant proportionality dependent on the curvature of the trajectory. At large time spans, it has been shown in isotropic turbulence that the mean curvature angle approaches $\pi/2$ indicating that all directions are equally probable in the asymptotic limit. At intermediate times, an inertial range is observed, especially for high Re . It is hypothesized that this time evolution of the curvature angle may be modified in the presence of wall confinement, owing to the limited directions that a fluid particle can traverse. The asymptotic angle in such geometries may help quantify the effect of confinement and may be related to the porosity of the bed.

4.1. Particle tracking and curvature angle calculation

Each tracer particle is injected at the center of a control volume at t_0 . The initial Lagrangian tracer location $X(\mathbf{x}_{cv}, t_0)$ is the same as \mathbf{x}_{cv} , the center coordinates of the control volume which contains the tracer. In the following, X_0 is used to represent $X(\mathbf{x}_{cv}, t_0)$ for simplicity. The fluid velocity $\mathbf{u}_{cv}(t_0)$ at corresponding \mathbf{x}_{cv} is used as particle velocity $\mathbf{v}(X_0, t_0)$ at the first time step to advance tracers. After the initial time step, particle velocity $\mathbf{v}(X_0, t_i)$ is calculated using linear interpolation of the Eulerian velocity field $\mathbf{u}(t_i)$ to the particle location, and a RK4 scheme is implemented to advance the tracer locations. In this study, 10,000 particles are randomly released at the same time and tracked to collect the trajectories. The lifetime of each tracer is about 10 times the Lagrangian integral time scale, which ensures that the multiscale features could be captured in the post-processing analysis. This procedure is repeated 10 times to get a sufficiently large number of trajectories. Results of the curvature angle variation for $Re_p = 1000$ are obtained and discussed later.

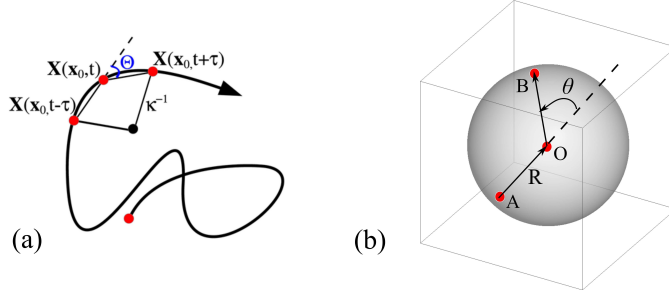


FIGURE 5. (a) Definition of curvature angle and (b) schematic of a block in a stochastic model.

4.2. A stochastic model

A Monte Carlo-based stochastic model to predict the long time behavior of the curvature angle is developed and its prediction is compared with the asymptotic value obtained from the Lagrangian particle tracking. It is hypothesized that this long time behavior of the curvature angle is dependent on the pore geometry. Mask functions (or filter functions), containing all possible angles ranging from 0 to π , represented by three points in a sphere (Figure 5(b)) are randomly placed and tested inside of the unit cell. Only those combinations are kept for which all three points lie within the fluid domain and the position vectors constructed by them also locate entirely within the fluid domain (and do not cross the solid region). This procedure is repeated to obtain a large sample (100,000 samples). The cosine of the angle is recorded for each valid realization and the mean value is calculated. Also, mask functions with different radii are checked to estimate the dimension influence on the mean angle. The algorithm can be summarized in two steps:

$$\cos(\theta) = \vec{AO} \cdot \vec{OB} / (|\vec{AO}| \cdot |\vec{OB}|). \quad (4.2)$$

(i) In order to simplify the filtering process, the sample blocks in a unit sphere need to be constructed first. Three points A, B and O (Figure 5(b)) are used to compose one pair of block, where A and B are on the surface of the sphere of the same radius R , while O is the center. Sufficiently large numbers of blocks are built in the sphere, so that each represents a unique combination of three points, but not necessarily a unique angle θ (Figure 5(b) and Eq 4.2). That is to say, different pairs of blocks could have the same angle. (Here θ is used as angles calculated by the stochastic model, in contrast to Θ , the curvature angle obtained from particle trajectories.) Consequently, it is critical to make each angle have the same probability in all blocks. The easiest way to build such a combination is to first find a list of points uniformly distributed on the sphere surface. Then, simply pair these points as A and B. At the same time, cosine of θ is calculated according to Eq 4.2. Finally, all the paired blocks and corresponding angles are stored.

(ii) The saved blocks are then used as filter functions placed inside the porous unit cell. The size of the filter function is adjusted by multiplying the coordinates of the blocks by a factor between 0 and 1. To determine whether one block is valid or not, two conditions must be satisfied. One is that all three points are inside the fluid domain. This is checked by calculating the minimum distance from each point to all bead centers. If the minimum distance of any three points is less than the radius of the bead, the pair of blocks is invalid. The other condition is that the blocks do not cross any solid regions. A multi-step geometric check is conducted to accommodate such requirements. On the periodic boundaries, periodicity is enforced in checking the spherical blocks.

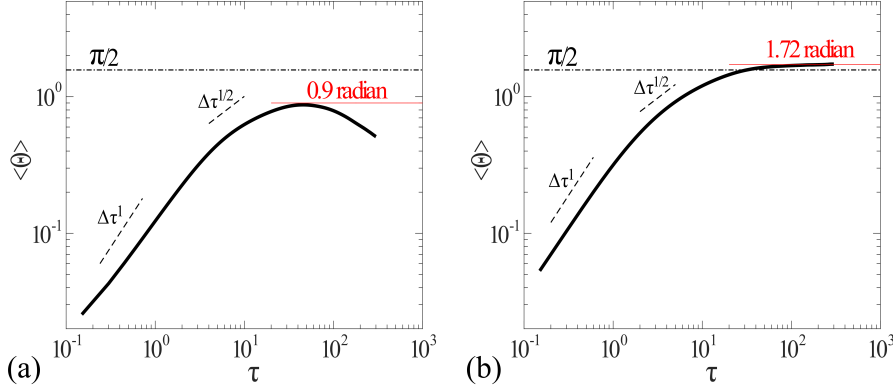


FIGURE 6. Ensemble averaged curvature angle Θ as a function of time lag $\Delta\tau$ calculated from trajectories of fluid particle evolving with (a) total velocity and (b) fluctuating velocity only.

4.3. Results and Discussion

The mean curvature angle $\langle\Theta\rangle$ is plotted against the time lag $\Delta\tau$ in a log-log scale in Figure 6. In order to assess the effect of mean flow on the curvature angle, especially on the asymptotic value, calculations are performed by advancing the fluid particles with total instantaneous velocity (Figure 6(a)) as well as by using just the fluctuating velocity where the mean was removed (Figure 6(b)). For both figures, the presence of two power laws is evident. In the short time span, a linear relationship is obtained; while in the inertial region, Θ is estimated to be correlated with $\Delta\tau^{1/2}$. And the inertial region is bounded by the kolmogorov time scale and integral time scale. The origins of these two power laws are discussed in Bos *et al.* (2015). Figure 6(a) shows that, at large times, the mean curvature angle increases, reaches a maximum of 0.9 radian and then decreases again. An asymptotic value is not observed as conjectured earlier, resulting from the strong mean flow effect. The mean flow stretches the trajectories in certain directions, reducing the possibilities for particles to go to other directions. The curvature angle obtained from tracking particles using only the fluctuations in fluid velocity, however, does provide an asymptotic value of 1.72 radian. This value is larger than $\pi/2$, a value obtained for isotropic turbulence and is a result of the flow confinement due to porous structure.

Figure 7 shows the evolution of mean angle θ computed from the stochastic model for different radii, R , of mask functions, where R is normalized with the hydraulic diameter D_h of the porous media. It is seen that the mean angle starts with $\pi/2$ for low R , indicating that all directions are equally likely for small radius of the masking function. θ increases with increasing R , reaches a first maximum at $\frac{R}{D_h} = 1$, then decreases and again reaches a maximum for R equal to the length of the unit cell. The physical meaning of these two maxima is being investigated; however, it shows that with increasing R , all directions are not equally likely, owing to the influence of porous geometry. Nevertheless, it is seen that for large R , the mean angle approaches 1.724 radian, which is very close to the asymptotic value obtained at large times for particles advanced by fluctuating fluid velocity only, as shown in Figure 6(b). The reason for this is that the stochastic model does not consider the directionality of the mean flow. As a result, it is only geometrically dependent. Hence, matching of the asymptotic angle obtained from the fluctuation velocity field is to be expected. That this value is different from $\pi/2$, as observed in isotropic turbulence, indicates the effect of porous geometry used in the study. Further

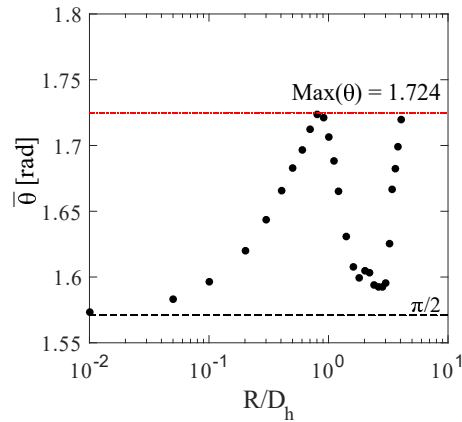


FIGURE 7. Averaged curvature angle θ as a function of mask function radius R normalized by hydraulic diameter.

modifications of the stochastic model are necessary to predict the long time behavior of the curvature angle when mean flow is also considered.

5. Summary and conclusion

A fully resolved direct numerical simulation was performed on a face-centered porous unit cell using a Cartesian grid-based fictitious domain method. In order to better understand the multiscale feature of fluid flow in pore-scale, both Eulerian and Lagrangian statistics were computed. For this porous arrangement with very low porosity, a large acceleration and deceleration flow was obtained. Negative production of turbulent kinetic energy was found both at the entrance and exit regions of the center pore, which mainly comes from the spanwise acceleration and streamwise deceleration of the mean flow. The time evolution of mean curvature angle obtained from the Lagrangian tracer trajectories was calculated and a Monte Carlo-based stochastic model was developed to predict the mean asymptotic curvature angle at large time spans. The asymptotic mean curvature angle obtained from trajectories of particles evolving with fluctuation velocity was accurately predicted by the stochastic model. Further modifications to the stochastic model are needed to account for the influence of the mean flow.

Acknowledgments

The authors acknowledge use of computational resources from the Certainty cluster awarded by the National Science Foundation to CTR. The authors are grateful to Prof. Ali Mani for hosting the present research work. The authors thank Dr. Amin Doostmohammadi for his insightful comments on the manuscript. Partial funding from NSF award #1336983 is also acknowledged.

REFERENCES

- ANDRIGO, P., BAGATIN, R. & PAGANI, G. 2000 Fixed bed reactors. *Catalysis Today* **52**, 197–222.
- ANTOHE, B. & LAGE, J. 1997 A general two-equation macroscopic turbulence model for incompressible flow in porous media. *Int. J. Heat Mass Tran.* **40**, 3013–3024.

- APTE, S., MATHIEU, M. & PATANKAR, N. 2008 A numerical method for fully resolved simulation (FRS) of rigid particle-flow interactions in complex flows. *J. Comput. Phys.* **228**, 2712–2738.
- BOS, W., KADOCH, B. & SCHNEIDER, K. 2015 Angular statistics of Lagrangian trajectories in turbulence. *Phys. Rev. Lett.* **114**, 1–5.
- DIXON, A. & CRESSWELL, D. 1986 Effective heat transfer parameters for transient packed-bed models. *AIChE J.* **32**, 809–819.
- EIGENBERGER, G. 1992 *Fixed-Bed Reactors*. Wiley Online Library.
- ERGUN, S. 1952 Fluid flow through packed columns. *Chem. Eng. Prog.* **48**, 89–94.
- GUNN, D. 1987 Axial and radial dispersion in fixed beds. *Chem. Eng. Sci.* **42**, 363–373.
- HAERI, S. & SHRIMPTION, J. 2011 A mesoscopic description of polydispersed particle laden turbulent flows. *Prog. Energy Combust. Sci.* **37**, 716–740.
- HILL, R. & KOCH, D. 2002 The transition from steady to weakly turbulent flow in a close-packed ordered array of spheres. *J. Fluid Mech* **465**, 59–97.
- HLUSHKOU, D. & TALLAREK, U. 2006 Transition from creeping via viscous-inertial to turbulent flow in fixed beds. *J. Chromatogr.* **A1126**, 70–85.
- JUSTIN, F. & APTE, S. 2013 Relative performance of body fitted and fictitious domain simulations of flow through packed beds. *Int. J. Multiphase Flow* **56**, 54–71.
- LEMONS, M. & PEDRAS, M. 2001 Recent mathematical models for turbulent flow in saturated rigid porous media. *J. Fluids Eng.* **123**, 935–940.
- MASUOKA, T. & TAKATSU, Y. 1996 Turbulence model for flow through porous media. *Int. J. Heat Mass Transfer* **39**, 2803–2809.
- NAKAYAMA, A. & KUWAHARA, F. 1999 A macroscopic turbulence model for flow in a porous medium. *J. Fluids Eng.* **121**, 427–433.
- NISHINO, K., SAMADA, M., KASUYA, K., & TORII, K. 2008 Turbulence statistics in the stagnation region of an axisymmetric impinging jet flow. *Int. J. Heat Fluid Flow* **17**, 193–201.
- PATIL, V. & LIBURDY, J. 2013 Turbulent flow characteristics in a randomly packed porous bed based on particle image velocimetry measurements. *Phys. Fluids* **25**, 043304.
- PEARSON, J. & TARDY, P. 2002 Models for flow of non-Newtonian and complex fluids through porous media. *J. Non-Newtonian Fluid Mech.* **102**, 447–473.
- PEDRAS, M. & LEMONS, M. 2001 Macroscopic turbulence modeling for incompressible flow through undeformable porous media. *Int. J. Heat Mass Tran.* **44**, 1081–1093.
- POPE, S. 2000 *Turbulent Flows*. Cambridge University Press.
- SUGA, K. 2016 Understanding and modeling turbulence over and inside porous media. *Flow Turbul. Combust/* **96**, 717–756.
- UTH, M., JIN, Y., KUZNETSOV, V., & HERWIG, H. 2016 A direct numerical simulation study on the possibility of macroscopic turbulence in porous media: Effects of different solid matrix geometries, solid boundaries, and two porosity scales. *Phys. Fluids* **28**, 065101.
- WEN, C. & FAN, L. 1975 *Models for flow systems and chemical reactors*. Marcel Dekker, Inc., New York.
- ZHOU, J., ADRIAN, R., BALACHANDAR, S. & PATANKAR, N. 2008 A numerical method for fully resolved simulation (FRS) of rigid particle-flow interactions in complex flows. *J. Comput. Phys.* **228**, 2712–2738.